Characterizing the Nova600 microfocus X-ray sourc for use with the Talbot interferometer for phase-contrast imaging

Miriam Robinson

Department of Physics, Lewis & Clark College, Portland, Oregon, 97219

(Dated: August 19, 2010)

The limitations of the Talbot interferometer for use with the Nova600 microfocus X-ray source are discussed. The spatial resolution and the phase sensitivity of the system are calculated. The resolution takes into account the Nova600's source size, Fresnel diffraction limits and phases grating period. The phase sensitivity is determined through Monte Carlo simulation.

1. INTRODUCTION

X-ray imaging has become essential to many medical and technical application, but there have been few advancements in the technique. The X-ray imaging we see done in the doctor's office is based on absorption contrast, which provides little information on weakly-absorbing or thin materials. Recently, phase-sensitive X-ray imaging has become a prominent area of research because it is sensitive to slight variations in the density of matter and has the potential to be used with existing X-ray sources.

We have constructed a Talbot interferometer for phase-contrast imaging, which we have been using at the F3 station at the Cornell High Energy Synchrotron Source (CHESS). We have ordered the Nova600 microfocus X-ray source from Oxford Instruments so that we can image when we do not have beam time and take quick images of a specimen in order to determine if it has interesting features. While the Nova600 has less flux than the synchrotron, it has a smaller source size, which may increase the visibility. We wish to determine the capabilities of the Nova600 and so we have estimated the resolution and phase sensitivity of the Talbot interferometer with the microfocus source.

2. BACKGROUND

The Talbot interferometer is based on the self-imaging "Talbot effect" [1]. When a monochromatic light source passes through a diffraction grating it forms periodic self-images at certain distances downstream. Fig. 1 illustrates the concept of the Talbot interferometer. A silicon phase grating, g_1, is placed a distance L downstream of the source. A highly absorbing, gold-coated analyzer grating, g_2, is placed a fractional Talbot distance behind g_1 [2],

$$d_m = m\frac{p_1{}^2}{8\lambda},\tag{1}$$

for a parallel beam setup, where m is an odd integer corresponding to the order of the Talbot distance, and λ is the wavelength. For our cone beam setup, the fractional Talbot distance is given by

$$d_m{}^* = \frac{L}{L - d_m}d_m.\tag{2}$$
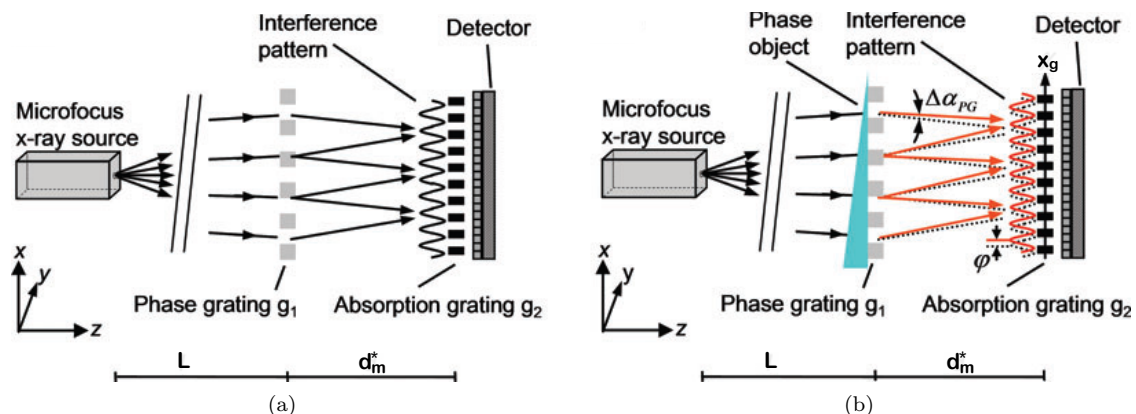
FIG. 1: Talbot interferometer for phase-contrast imaging. (a) The setup without a sample. The phase grating, g_1, acts as a beam splitter and the diffracted light forms an interference pattern at the analyzer grating, g_2. (b) The setup with a sample in the beam path. The sample shifts the angle of diffraction by $\Delta\alpha_{PG}$ and shifts the interference pattern by φ [2].

g_1 is a π-shifting phase grating that acts as a beam splitter, dividing the beam into the +1 and -1 diffractive orders. The diffracted light forms an interference pattern at g_2. The period of g_2 (p_2) is matched to the period of the fringes. $p_2 = p_1/2$, for a parallel beam setup, and

$$p_2{}^* = \frac{L}{L - d_m} \frac{p_1}{2},$$ (3)

for a cone beam setup [2].

For our setup p_2 is fixed at 2μm, so it is useful to solve for p_1:

$$p_1 = \frac{2(L - d_m)}{L} p_2.$$ (4)

Using equation (1), we get

$$p_1 = \frac{2(L - m\frac{p_1{}^2}{8\lambda})}{L} p_2$$

simplifying, we get

$$Lp_1 = 2L - m\frac{p_1{}^2}{4\lambda} p_2 0 = m\frac{p_2}{8\lambda} p_1{}^2 + Lp_1 - 2Lp_2$$

and thus

$$p_1 = \frac{2(L - d_m)}{L} p_2$$

$$\stackrel{(1)}{\Rightarrow} \quad p_1 = \frac{2(L - m\frac{p_1{}^2}{8\lambda})}{L} p_2$$

$$\text{simplifying,} \quad Lp_1 = 2L - m\frac{p_1{}^2}{4\lambda} p_2$$

$$\Rightarrow \quad 0 = m\frac{p_2}{8\lambda} p_1{}^2 + Lp_1 - 2Lp_2$$

$$\Rightarrow \quad p_1 = \frac{-L + \sqrt{L^2 + 4m\frac{p_2}{4\lambda} 2p_2 L}}{2m\frac{p_2}{4\lambda}}$$

$$= \frac{-L + \sqrt{L^2 + 2Lm\frac{p_2{}^2}{\lambda}}}{m\frac{p_2}{2\lambda}}$$

$$= 2\frac{\lambda}{mp_2} \left(-L + \sqrt{L^2 + 2L\frac{mp_2{}^2}{\lambda}} \right).$$ (5)

Then, given L, equation (5) can be used to calculate $d_m{}^*$.

When a sample is placed in the beam path, the angle of diffraction is shifted by $\Delta\alpha_{PG}$ at the phase grating [2]

$$\Delta\alpha_{PG} = \frac{\lambda}{2\pi} \frac{\partial\Phi}{\partial x},$$

where $\frac{\partial\Phi}{\partial x}$ is the differential phase shift at g_1 due to the sample. This causes a shift in the interference pattern [2]

$$\varphi = \frac{\lambda d_m}{p_2} \frac{\partial\Phi}{\partial x}.$$ (6)

We can determine the position of the interference pattern at g_2 by running a phase-stepping scan, in which we shift the analyzer grating along x_g (see Fig. 1) through one period of g_2. Since g_2 is highly absorbing and period-matched to the fringes, the phase-stepping scan causes the the intensity in each pixel (m, n) to oscillate sinusoidally (Fig. 2) according to [3]

$$I(m, n, x_g) = \sum_i a_i(m, n) \cos(i2\pi x_g/p_2 + \varphi_i(m, n))$$

$$\approx a_0(m, n) + a_1(m, n) \cos(2\pi x_g/p_2 + \varphi_1(m, n)),$$ (7)

where a_i are amplitude coefficients and φ_i are phase coefficients. By repeating the process without the sample in the beam, we can detect the changes due to the sample and reconstruct an image using a discrete Fourier transform (DFT) or a curve fitter. Absorption-contrast images can be obtained from the change in the average intensity a_0. Dark field images can be obtained from examining the decrease in the ampliude of oscillation a_1 due to scattering. And differential phase-contrast images can be obtained by examining the shift of the interference fringes φ_1.
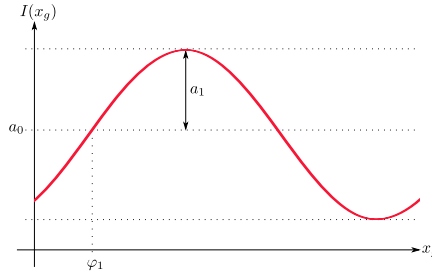
FIG. 2: Intensity in a pixel as g_2 is scanned along x_g. The extracted parameters a_0, a_1 and φ_1 can be compared to a reference scan to obtain absorption, dark field and phase-contrast images.

3.   RESOLUTION

We wish to determine the minimum detectable feature for the Talbot interferometer with the new Oxford Instruments Nova600 microfocus X-ray source.

3.1.   Limits

The resolution of the system is limited by the finite source size, Fresnel diffraction limits, and the period of the phase grating. Fig. 3 outlines the geometry that limits the resolution of the Talbot interferometer.

3.1.1.   Source size

The Nova600 has a Gaussian source size of 13-20μm (FWHM), according to the specifications given by Oxford Instruments. We used the highest source size, 20 μm, in order to estimate the worst visibility. The projected source size at the analyzer grating is

$$\Sigma_p = \Sigma \left(\frac{d_m{}^*}{L} \right) \tag{8}$$

where Σ is the source size and $d_m{}^*$ is the distance between the source and the analyzer grating.

The source size limits the fringe visibility at the detector. The convolution of a perfect sine wave with the Gaussian source profile yields an equation for the visibility [4]

$$\begin{aligned} V &= e^{-(1.887\Sigma_p/p_2)^2} \\ \overset{(8)}{\Rightarrow} \quad V &= e^{-(1.887\Sigma d_m{}^*/Lp_2)^2}. \end{aligned} \tag{9}$$
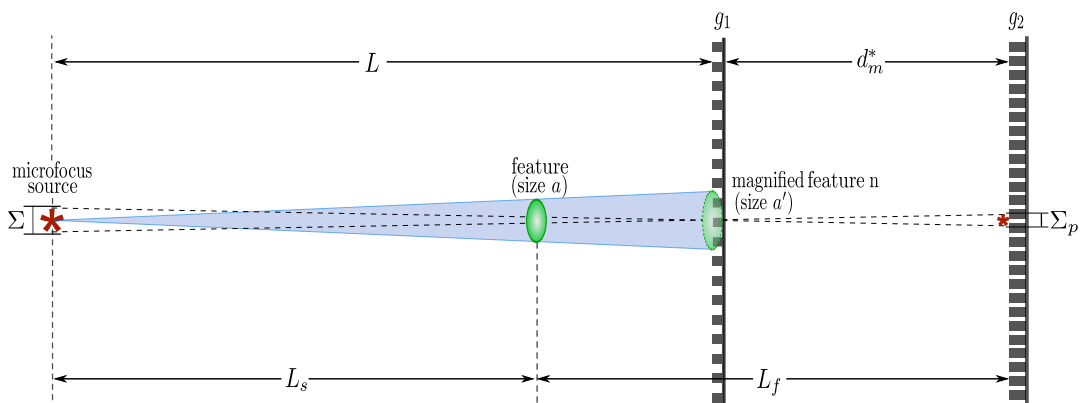
FIG. 3: Setup of the Talbot interferometer. L and L_s are the distances from the source to the phase grating and specimen, L_f is the distance from the specimen to the analyzer grating, $d_m{}^*$ is the inter-grating distance (a fractional Talbot distance of order m for a cone beam), s is the source size, w is the projected source size, a is the size of the specimen, a' is the effective size of the specimen, and g_1 and g_2 are the phasing and analyzer gratings.

Momose *et al.* [5] believe that a fringe visibility of at least 0.2 is needed for quantitative phase measurement. However, imaging has been achieved with a visibility of 0.03-0.05 [6, 7]. We will use 0.2 as a reasonable minimum visiblity, but we will also calculate the resolution for minimum visibility of 0.03 for a very optimistic estimation.

3.1.2. *Fresnel diffraction limits*

Since the Talbot effect is a near-field diffraction effect, the geometry of the system must maintain $F \gtrsim 1$, where F is the Fresnel number. For our system, F is defined as

$$F = \frac{a^2}{\lambda L_f} \tag{10}$$

where a is the size of the feature of interest and L_f is the distance between the specimen and the analyzer grating.

3.1.3. *Phase grating period*

Since the phase data from the specimen will be imprinted in the interference pattern at g_1, the smallest amount of information we can have will be contained within one fringe. Then the feature of interest should be magnified so that it is comparable to p_1 at the phase grating. As L increases, p_1 approaches that given by a parallel beam setup (see Fig. 4, $p_1 = 2p_2$. And since p_2 is fixed at 2 μm, the limit for p_1 is 4 μm. Thus a' should be $\sim 4\mu$m at g_2.

The magnification due to a cone beam at the phase grating is given by

$$M = \frac{L}{L_s} \tag{11}$$

where L_s is the distance between the source and the specimen. Thus the effective feature size at the phase grating is

$$a' = Ma. \tag{12}$$
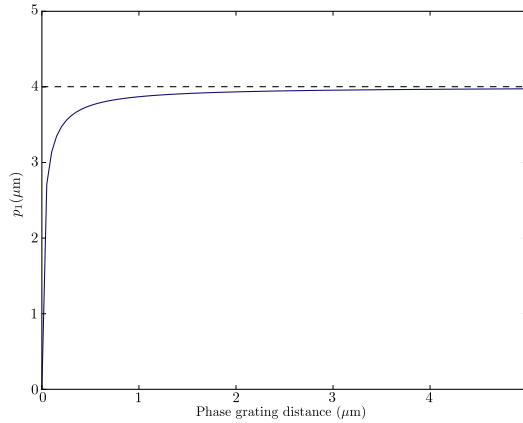
FIG. 4: The phase grating period, p_1, as a function of the phase grating distance, L. As L increases, the beam becomes more like a parallel beam and p_1 approaches $p_2 = p_1/2 = 4\mu$m.

In summary, g_1 must be far enough from the source to achieve a minimum required visibility. The specimen must be close enough to g_2 to stay within the Fresnel diffraction region. But it must also be far enough from g_1 to be magnified to 4μm at g_1.

3.2. Results

Since the geometry of the system depends on the periods of the gratings, and p_2 is fixed at 2μm, we can take various values for L and L_s and calculate $d_m{}^*$, and thus calculate V, F, and a' for a specific feature size. From this we can find the region defined by our limitations and find the maximum phase grating distance for that feature size. The maximum phase grating distance can be used to calculate the best obtainable visibility.

Python and matplotlib were used to generate plots approximating the distances L and L_s at which $a' \approx 4\mu$m and $F \approx 1$ for different feature sizes, a, at the first fractional Talbot distance (m=1). The value of L at intersection of these functions can be used to calculate the best V obtainable within the Fresnel and magnification limits. Obtaining the best visibility for a range of feature sizes (2-4μm), we were able to plot the best visibility versus a (see Fig. 5). Calculations were made for a 22keV beam with a 20μm source size.

With a minimum required visibility of 0.03, the minimum detectable feature size is $\sim 2.3\mu$m. And with a minimum required visibility of 0.2, the minimum detectable feature size is $\sim 2.8\mu$m. Thus the theoretical minimum detectable feature is 2.3-2.8μm.
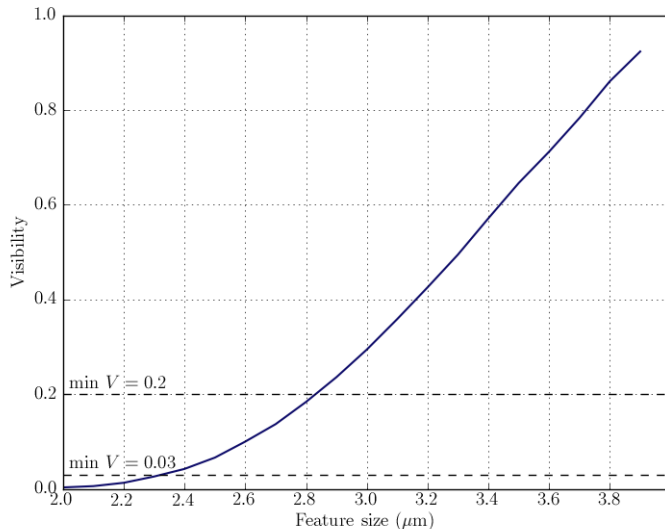
FIG. 5: Best visibility obtainable as a function of feature size a. The dashed lines indicated the two different suggested minimum visibilities. For a minimum required visibility of 0.03, the minimum detectable feature is $\sim 2.3\mu$m. For a minimum required visibility of 0.2, the minimum detectable feature is $\sim 2.8\mu$m.

4. SENSITIVITY

We wish to estimate the sensitivity of the Talbot interferometer to the phase difference caused by a sample with the new microfocus source. This is determined by the amount noise inherent in the system.

4.1. Uncertainty

4.1.1. Counting statistics

The error due to counting statistics contributes the most uncertainty to the extracted phase. Thus if the detector records N_e electrons in one pixel, the uncertainty in that recorded signal is $\sigma_e = \sqrt{N_e}$. By increasing the imaging time we can increase the number of incident photons, increasing N_e, and thus reduce the relative uncertainty $\sqrt{N_e}/N_e = 1/\sqrt{N_e}$ as much as our time schedules allow.

4.1.2. Dark current

Even without any incident photons, the detector accumulates a number of counts, N_d, due to the random generation of electron hole pairs. They are also subject to Poisson statistics and have an uncertainty of $\sqrt{N_d}$, which adds to the total uncertainty. At F3 this contribution is negligible, however, we need to determine if this has a significant contribution when using the Nova600.

We have measured a pixel response of $\sim 3e^-$ per incident photon for our Finger Lakes CCD detector, so the number of recorded electrons due to incident X-rays is $N_{X-ray} = 3e^-/\text{ph} \cdot N_p$, where N_p is the number of incident photons. The Nova600 has a quoted flux of 1.1×10^{12} ph/sec/sr at 60W. At 22keV, the interferometer is predicted to transmit 30% of the incident flux, making the average flux about 3.5×10^{11} ph/sec/sr. If our camera has an effective pixel size of 6.25μm and we image at a working distance of D meters, then, on average, each pixel recieves a flux of

$$
\begin{aligned}
N_p &= \frac{(6.26\mu\text{m})^2}{D^2}\text{sr} \cdot 3.5 \times 10^{11} \text{ ph/sec/sr} \\
&= \frac{13.67\text{m}^2}{D^2} \text{ ph/sec}. \tag{13}
\end{aligned}
$$

Due to limited space, the maximum working distance will likely be ~ 1.5m. At $D = 1.5$m, $N_p = 6.08$ph/sec. Then, if a pixel receives the average flux, the detector will record $(3e^-/\text{ph}) \cdot (6.08\text{ph/sec}) = 18.24e^-/\text{sec}$. Now, the dark accumulation is $0.30e^-/\text{pixel/sec}$ [8]. Then we have more than enough incident photons per second to stay ahead of the dark current. Thus the uncertainty due to dark current does not contribute significantly to the total uncertainty, and we can neglect it.

4.2. Monte Carlo Simulation

We simulated the recovery of the amplitude and phase data for a sinusoid with added noise with a Monte Carlo simulation in order to estimate the phase sensitivity of the interferometer. Since we have the option of using a DFT or curve fitter, we used both methods in the simulation. The DFT is generally faster than fitting to a curve, but the

parameters extracted by the curve fitter are more correct. Using both allowed us to compare the sensitivities of the methods as well as determine the sensitivity of the system.

4.3. Method

We used the following method to estimate the phase sensitivity:

- Create a perfect sinusoid $a_0 + a_1 \sin(2\pi x + \varphi)$ and sample N equally spaced points (the number of images in a phase-stepping scan)

- Add Gaussian noise with standard deviation σ_e (calculated as $\sqrt{N_e}$ for each point)

- Apply the DFT to the noisy points

- Recover estimated a_0, a_1 and φ

- Repeat many times (we used about 100,000 trials). Calculate the standard deviation of all the extracted φ, which gives a reasonable estimate of the sensitivity.

- Repeat for curve fitter

4.4. Results

To simulate a pixel with 100% visibility, we set $I_{min} = 0$ ADU. Our detector digitalizes images to 16 bits per pixel, so the maximum intensity the detector can read out is 2^{16} - 1 = 65535 ADU. The minimum intensity the detector can read out is 10400 ADU. Thus, if we want to set $I_{min} = 0$ ADU, then $I_{max} = 55135$ ADU. Then our sinusoid will have a_0, $a_1 = 27567.5$.

We ran the Monte Carlo simulation with 100,000 trials for $N = 5$-19, each time with a_0, $a_1 = 27567.5$ and $\varphi = 0$, with both the DFT and curve fitter. By increasing the number of sampled points we can further constrain the sinusoid, so the uncertainty improves as N increases. Fig. 6 shows the dependence of the uncertainty $\Delta\varphi$ on the number of sampled points N for the DFT and curve fitter. We can see that the uncertainty for the curve fitter, $\Delta\varphi_{curve}$, is consistently smaller than the uncertainty for the DFT $\Delta\varphi_{DFT}$, although the difference becomes smaller as N increases. For $N = 5$, $\Delta\varphi_{curve} = 3.56 \times 10^{-3}$ and $\Delta\varphi_{DFT} = 4.27 \times 10^{-3}$. The difference is smaller for $N = 11$, where $\Delta\varphi_{curve} = 2.48 \times 10^{-3}$ and $\Delta\varphi_{DFT} = 2.70 \times 10^{-3}$. By $N = 19$, $\Delta\varphi_{curve} = 1.91 \times 10^{-3}$ and $\Delta\varphi_{DFT} = 2.01 \times 10^{-3}$, and there is little difference.
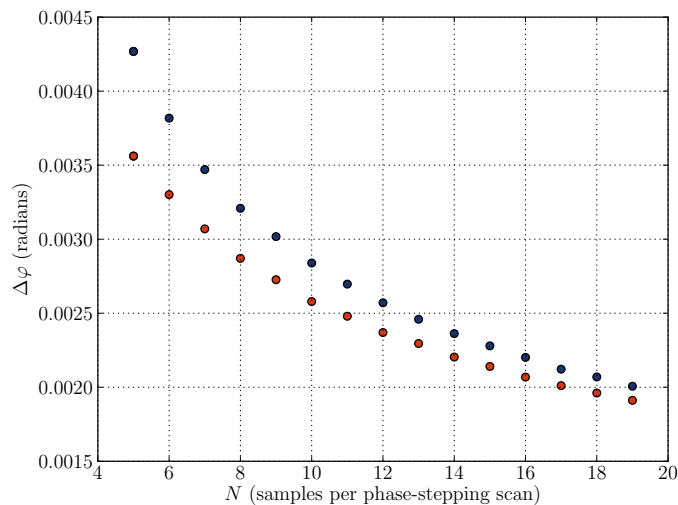
FIG. 6: Plot of the standard deviation of the recovered phase versus N, the number of images in a phase-stepping scan. Blue points were retrieved from the DFT and red points from the curve fitter.

4.5. Analysis

The refractive index for X-rays is slightly less than 1 for all materials, so we express the complex refractive index as $n = 1 - \delta + i\beta$. Since we are considering weakly absorbing samples, the absorption index β is very small compared to δ. Thus we consider only δ in our analysis.

Assume we are taking a knife-edge profile of the transmitted beam in which we step a straight-edge across the analyzer grating plane and measure the intensity for each step. If we are imaging a bug in amber, let's say we take a knife-edge step from amber (δ_A) to bug (δ_B). Since the Nova600 has a Gaussian source profile, when convolved with

the projected source size Σ_p (FWHM), the knife-edge is smeared over a distance Σ_p (see Fig. 7). Then the decrement profile is approximately

$$\delta \approx \delta_A + \frac{\delta_B - \delta_A}{\Sigma_p} \cdot x$$

from $0 \leq x \leq \Sigma_p$. Then, as it travels through the specimen, the beams acquires a phase of [9]

$$\Phi(x) = \frac{2\pi}{\lambda} \int \delta(x) dz = \frac{2\pi}{\lambda} \int_A \delta_A dz + \frac{2\pi}{\lambda} \int_B \frac{\delta_B - \delta_A}{\Sigma_p} \cdot x dz,$$

where $\int_A$ and $\int_B$ indicate integration over the the thickness of the amber and bug. If we assume that the amber has been polished so that $\frac{\partial}{\partial x} \int_A \delta_A dz = 0$, then the differential phase shift caused by the specimen is

$$\frac{\partial \Phi}{\partial x} = \frac{2\pi}{\lambda} \int_B \frac{\delta_B - \delta_A}{\Sigma_p} dz = \frac{2\pi}{\lambda} \frac{\delta_B - \delta_A}{\Sigma_p} \cdot T_B,$$

where T_B is the thickness of the bug in the beam direction.

Then, assuming $p_1 \approx 2p_2$, the phase shift recorded by the detector is

$$\varphi = \frac{\lambda d_m}{p_2} \frac{\partial \Phi}{\partial x} = 2\pi \frac{m p_2}{2\lambda \Sigma_p} (\delta_B - \delta_A) \cdot T_B. \tag{14}$$

We can estimate the minimum detectable phase difference φ_{min} by doubling the uncertainty as found above (for either the DFT or curve fitter) in order to ensure that neighboring uncertainties do not overlap. If we rearrange equation (14), we can relate the detectable decrement difference $(\delta_B - \delta_A)$ to the minimum resolvable phase shift:

$$(\delta_B - \delta_A) T_B = \frac{\varphi_{min}}{2\pi} \frac{2\lambda \Sigma_p}{m p_2}. \tag{15}$$

Let $\lambda = 0.564$Å (22keV), $p_2 = 2\mu$m, and $\Sigma = 20\mu$m. If we want to work at $L = 1.5$m, then by equations (8) and (5), $\Sigma_p = m \cdot 0.462\mu$m. Fig 8 plots the detectable decrement difference versus T_B for $N = 5$, $N = 11$ and $N = 19$. This plot can be used to determine the minimum decrement difference given a thickness or the minimum thickness for a given decrement difference.
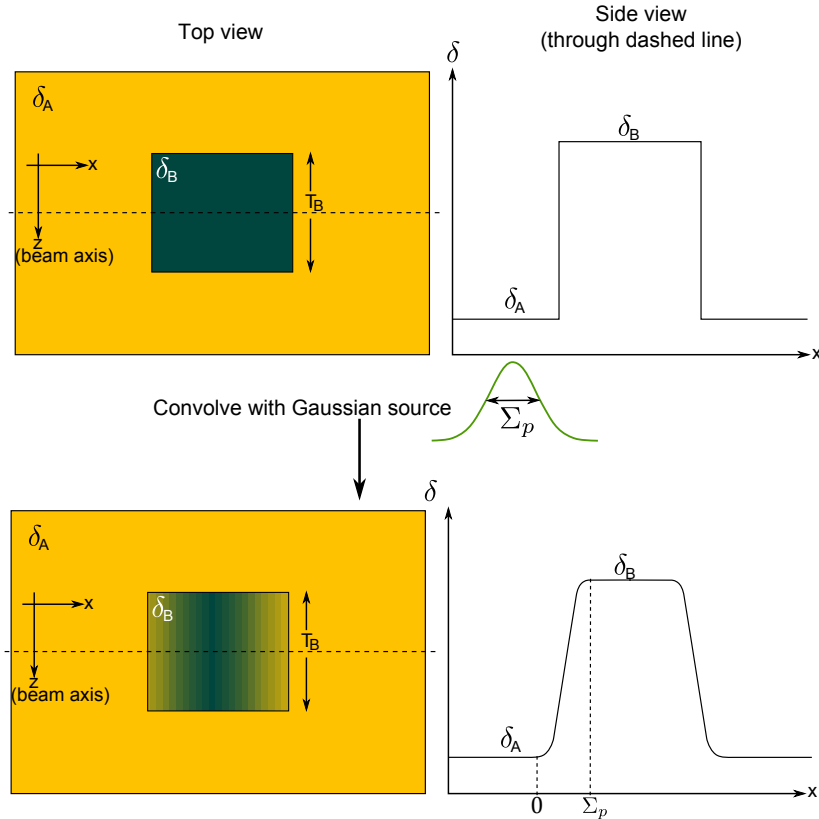
FIG. 7: Representation of the convolution of the Gaussian source profile with the decrement profile.
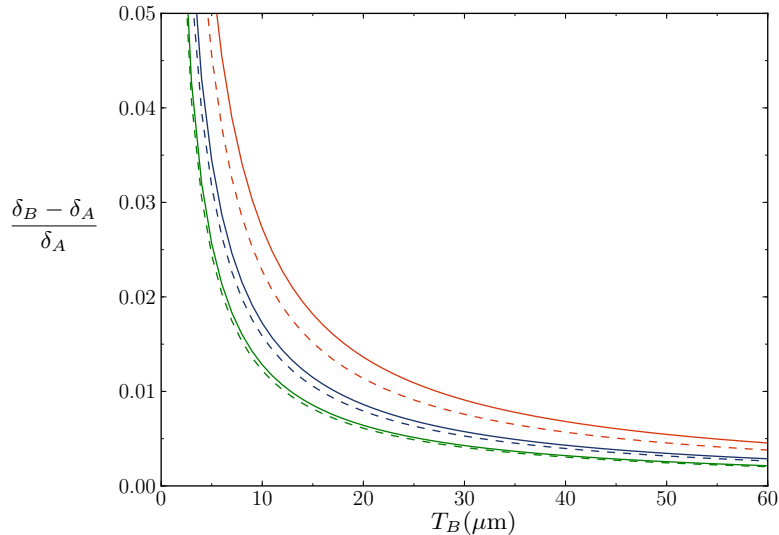
FIG. 8: Plot of the detectable decrement as a fraction of $\delta_A \sim 1.3 \times 10^{-6}$ versus feature thickness for $N = 5$ (red), $N = 11$ (blue), and $N = 19$ (green). Solid lines were obtained from the DFT and dashed lines were obtained from the curve fitter.

5. CONCLUSION

We determined the expected behavior of the Talbot interferometer when used with the Nova600 microfocus X-ray source. The resolution of the system is limited by the source size, Fresnel diffraction limits and the phase grating period. The resolution was calculated to be 2.3-2.8μm. Monte Carlo simulations were used to determine the uncertainty in the extracted phase shift using the DFT and curve fitter, which gives an estimate of the minimum resolvable phase difference. We analyzed the example of a bug in amber and plotted the minimum detectable decrement difference versus bug thickness. These calculations will allow us the determine which samples are suitable for imaging with the Talbot interferometer.

[1] H. Talbot, Philos. Mag. **9**, 401 (1836).
[2] M. Engelhardt, C. Kottler, O. Bunk, C. David, C. Schroer, J. Baumann, M. Schuster, and F. Pfeiffer, J. Microsc. **232**, 145 (2008).
[3] F. Pfeiffer, M. Bech, O. Bunk, P. Kraft, E. F. Eikenberry, C. Brönnimann, C. Grünzweig, and C. David, Nature Mater. **7**, 134 (2008).
[4] T. Weitkamp, C. David, C. Kottler, O. Bunk, and F. Pfeiffer, Proc. SPIE **6318**, 63180s (2006).
[5] A. Momose, Y. Wataru, H. Maikusa, and Y. Takeda, Opt. Express **17**, 12540 (2009).
[6] T. Weitkamp, B. Nöhammer, A. Diaz, and C. David, Appl. Phys. Lett. **86**, 054101 (2005).
[7] T. Donath, F. Pfeiffer, O. Bunk, M. Bednarzik, C. Grünzweig, E. Hempel, S. Popescu, M. Hoheisel, and C. David, Rev. Sci. Instrum. **80**, 053701 (2009).
[8] M. Tate, D. Chamberlain, and S. Gruner, Rev. Sci. Instrum. **76**, 083101 (2005).
[9] W. Yashiro, Y. Takeda, and A. Momose, J. Opt. Soc. Am. A **28**, 2025 (2008).